Please cite this paper as:

Li J, Shen J and Zhu S (2023). Adaptive Self-powered Active Vibration Control to Cable Structures. *Mechanical Systems and Signal Processing* 188: 110050.

https://doi.org/10.1016/j.ymssp.2022.110050

Adaptive Self-powered Active Vibration Control to Cable Structures

Jin-Yang LI, Jiayang SHEN, and Songye ZHU*

Department of Civil and Environmental Engineering, The Hong Kong Polytechnic University, Kowloon, Hong Kong, China

* Corresponding author: Dr. S. Zhu, Email: songye.zhu@polyu.edu.hk
mailto:ceszhu@polyu.edu.hk

ABSTRACT:

High-performance vibration control is always preferred for cable structures that are inherently flexible and susceptible to dynamic excitations. Among different control categories, active control generally surpasses the other types of control (i.e., passive, semi-active, etc.) in terms of control performance. However, its large energy consumption and the potential instability concern hinder its wide-spread applications in relevant fields. In this regard, we propose a novel power-oriented adaptive self-powered active control system to address these concerns without compromising active control performance. In particular, this study explores the full potential of the newly proposed system analytically and numerically via a case study of a 135 m full-scale bridge cable. Moreover, its control performance is meticulously compared with that of emerging passive control, namely, an optimal inerter damper. Simulation results confirm that the proposed system successfully realized considerably enhanced and broadband vibration mitigation performance than an optimal inerter damper without requiring an external energy supply. Slight modifications to the setup can further enable an easy transfer to other applications, shedding light on its promising future.

KEYWORDS:

Self-powered; Active control; Cable; Electromagnetic damper; *LQG* control; Inerter damper; Energy-neutral; adaptive control

Nomenclature:

Abbreviation	Full name
ARE	Algebraic Riccati Equation
EC	Energy Consumption
EH	Energy Harvesting
EM	Electromagnetic
ID	Inerter Damper
LQG	Linear Quadratic Gaussian
LQR	Linear Quadratic Regulator
MCU	Micro-Controller Unit
PID	Proportion–Integral–Derivative
PLC	Programmable Logic Controller
PWM	Pulse-Width Modulation
SPAC	Self-Powered Active Controller

1. INTRODUCTION

The inherent low damping coefficient of a cable makes it susceptible to external excitations (e.g., wind excitation). As a result, the cable may experience large vibration amplitude, which causes functionality and safety issues. Consequently, various control techniques have been proposed and implemented in cable structures to mitigate such undesired vibrations.

Existing control techniques are commonly categorized into four types: (1) passive control, (2) active control, (3) semi-active control, and (4) hybrid control [1]. In general, passive control has the widest applications, given its passive working mode and simplicity. Active control provides the best control performance at the cost of high energy consumption (i.e., requires external energy supply) and the requirement of feedback loops. Semi-active control achieves a balance between control performance and energy consumption by providing enhanced control over passive type while consuming energy that is orders less than active control. The remaining hybrid type is essentially a combination of the mentioned three types and inherits their pros and cons.

Nevertheless, the recent advances in energy harvesting (EH) techniques revolutionize the above conventional perception of the categorization because it can convert undesired vibrations in the form of kinetic energy into electrical energy that can be further stored and manipulated within the electrical domain. A reduction in system kinetic energy naturally leads to better control performance. Thus, dual purposes (i.e., energy harvesting and vibration control) can be simultaneously catered to; some recent review papers on this topic can be found in [2, 3]. For passive control, the feasibility of implementing a tuned mass damper (TMD) with an EH component in high-rise buildings was validated in [4, 5]; and a dual-function device was applied to cable vibration control in [6-8], where the harvested power is proved adequate to supply ambient sensors. The harvested energy can also be returned to the actuation system, which leads to semi-active control. Cho et al. [9, 10] and Chen and Liao [11] combined a magnetorheological (MR) damper with an electromagnetic (EM) device and validated that the energy harvested by the latter is sufficient to supply the former in establishing self-powered semi-active control.

Concerning the more attractive self-powered active control, prior trials can be generally divided into two groups. The first group functions similarly to the above self-powered semi-active control but involves a multi-location device arrangement. For example, Scruggs and Iwan [12] installed EH and active control units on the same structure and subsequently used the energy extracted from one location to support the active control process at another location where optimal control force is mostly required. Similarly, Suda et al. [13] realized self-powered active suspension of the secondary layer by utilizing the energy harvested from the primary layer (bottom layer). The second group involves alternative passive and active working modes. For instance, Tang and Zuo [14] utilized an active TMD to achieve clipped linear quadratic Gaussian (LQG) control algorithms. Jamshidi et al. [15, 16] developed self-powered semi-active control for cable structures using a hybrid electromagnetic damper. Following a similar approach, Chen et al.[17] realized a self-powered active vehicle suspension system.

Recently, the authors of this paper proposed the new concept of a self-powered active controller (SPAC) that enables authentic full-loop active control performance while harvesting energy (under certain circumstances). The feasibility of this device was cross-validated theoretically, numerically, and experimentally in an actively isolated structure presented in [18, 19]. This paper aims to extend this emerging active control technique to vulnerable cable structures for the first time to achieve optimal active control performance while remaining self-powered.

Studies on cables' active control can be traced to more than a decade ago. For instance, Fujino et al. [20] studied cable vibration control performance by actively adjusting the equivalent longitudinal stiffness based on the work in [21]. Thereafter, they extended their work to realize cable's active control via an axially movable support [22]. Active tendon controls on cable structure were studied in [23, 24]. A corresponding large-scale demonstration was subsequently conducted and reported in [25]. Similar studies on the application of active tendon control to suspension bridge cables were reported by the same group [26]. A systematic control performance comparison among passive control (i.e., negative stiffness damper), output feedback control, and active control using the linear quadratic regulator (LQR) was conducted in [27]. However, the energy and potential instability issues still prevent the in-situ adoption of active control for cable structures.

In this regard, this study aims to investigate the feasibility of implementing the SPAC system to the control of a full-scale cable model and, in particular, introduce a power-oriented active control strategy that will tackle both the aforementioned high-power consumption and potential instability issues. Hopefully, this study will promote the physical applications of active cable control in the near future and even be extended to other structural forms.

2. CABLE DYNAMICS UNDER TRANSVERSE CONTROL FORCE

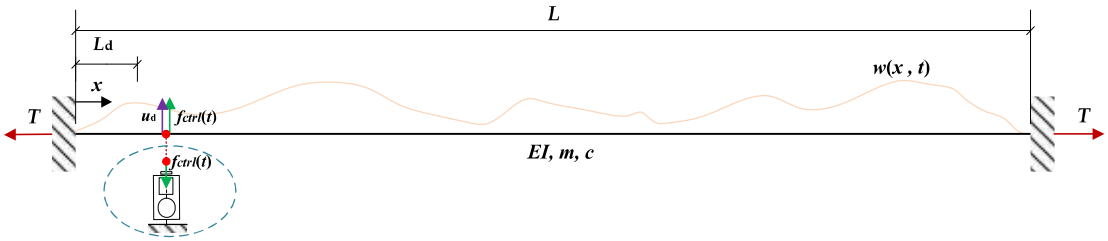

Fig. 1 Simplified schematic of a cable structure with a control device (transverse force)

Fig. 1 shows the corresponding schematic with the damper installed near the left anchorage providing control force in the transverse direction. Relevant cable parameters are subsequently defined as L = cable length, L_d = damper location (measured from the near-end anchorage), T = cable tensile force, m = mass per unit length, c = damping per unit length, EI = flexural rigidity, $w(x, t)$ = external excitation at location x and instant t, and $f_{ctrl}(t)$ = force provided by the external damper/actuator.

By referring to [28], the transverse dynamics of the cable under a single-point control can be written as

$$T\frac{\partial^2 u(x,t)}{\partial x^2}-\frac{\partial^2}{\partial x^2}\left(EI\frac{\partial^2 u(x,t)}{\partial x^2}\right)-c\frac{\partial u(x,t)}{\partial t}-m\frac{\partial^2 u(x,t)}{\partial t^2}=f_{\text{ctrl}}(t)\delta\left(x-L_{\text{d}}\right)+w(x,t) \tag{1}$$

,

where $u(x,t)$ = transverse displacement at location x and instant t, and $\delta(\cdot)$ = the Dirac delta function.

However, because Eq. (1) cannot be analytically solved, a finite difference method [29] is adopted in this paper to discretize the cable into lumped mass (**M**), stiffness (**K**), and damping (**C**) matrices, which can be subsequently used in the upcoming numerical simulations. If the cable is to be discretized into n+1 segments (n = 99 in the upcoming case study), then the corresponding discretized matrices can be subsequently obtained as

$$\mathbf{M} = \mathbf{I}_\mathbf{N} \cdot mq\,, \qquad \mathbf{K} = \begin{bmatrix} Q & D & W & & & 0 \\ D & S & D & W & & \\ W & D & S & D & \ddots & \\ & W & \ddots & \ddots & \ddots & W \\ & & \ddots & \ddots & S & D \\ 0 & & & W & D & Q \end{bmatrix}, \quad \mathbf{C} = \alpha\mathbf{M} + \beta\mathbf{K}\,, \tag{2}$$

where $\mathbf{I}_\mathbf{N}$ is an $n \times n$ identity matrix, q is the unit length (i.e., $q = L/(n+1)$), m is the mass per unit length, $S = 6EI/q^3 + 2T/q$, $D = -4EI/q^3 - T/q$, $W = EI/q^3$, $Q = 7EI/q^3 + 2T/q$ (for fixed end connection), and α and β are Rayleigh damping coefficients, respectively. The above notations slightly differ from the ones in [29] because we used absolute responses instead of normalized ones; the validity of this approach was successfully verified in the previous literature [27, 28].

Therefore, Eq. (1) can be rewritten in its matrix form as

$$\mathbf{M}\ddot{\mathbf{u}} + \mathbf{C}\dot{\mathbf{u}} + \mathbf{K}\mathbf{u} = \boldsymbol{\gamma} \cdot f_{\text{ctrl}} + \mathbf{w}\,, \tag{3}$$

where $\mathbf{u}$ is the response vector (displacements of all nodes), $\boldsymbol{\gamma}$ is the damper location assignment vector, and $\mathbf{w}$ is the external disturbance/excitation vector (i.e., wind load in this paper) in the form of

$$\begin{aligned} \mathbf{u} &= [u_1 \quad u_2 \quad \cdots \quad u_n]^\mathrm{T}, \\ \mathbf{w} &= [w_1 \quad w_2 \quad \cdots \quad w_n]^\mathrm{T}, \\ \boldsymbol{\gamma} &= [\gamma_1 \quad \gamma_2 \quad \cdots \quad \gamma_n]^\mathrm{T}, \\ \text{where} \quad \gamma_i &= \begin{cases} 0, & i \neq j \\ 1, & i = j \end{cases}. \end{aligned} \tag{4}$$

where u_i is the displacement response of the i^{th} node (i = 1, 2 …, n), w_i is the concentrated external force on the i^{th} node, and j is the node number with the damper.

3. SPAC

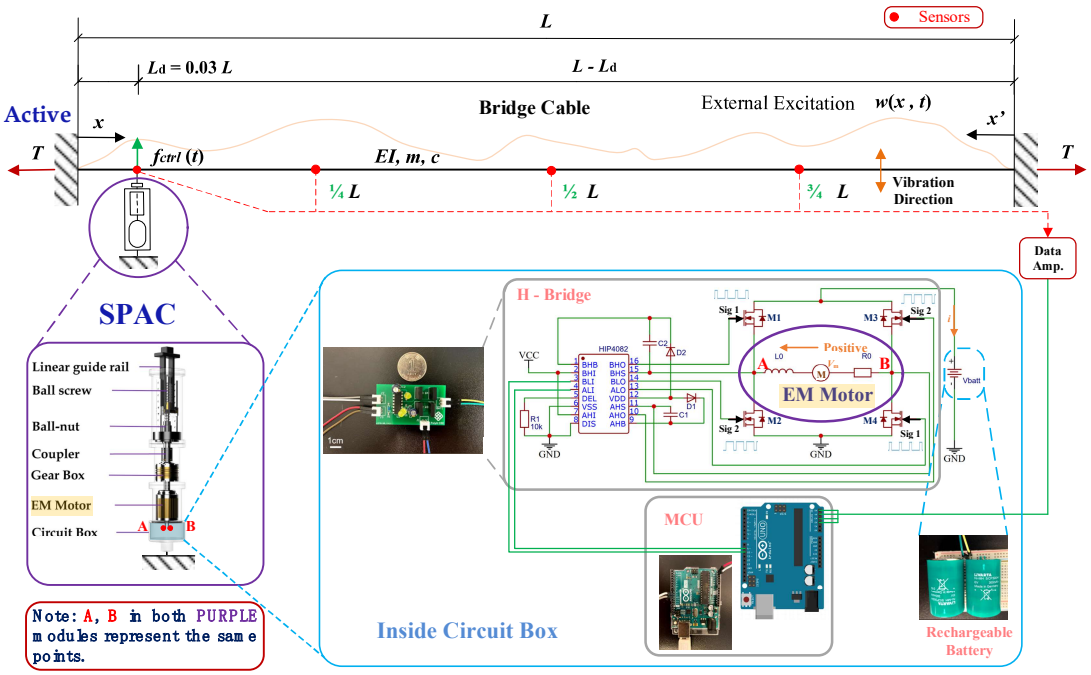

Fig. 2 Cable active control with SPAC

Fig. 2 adds more details to Fig. 1 by including both zoomed-in details of the SPAC and the sensor arrangement. The damper location is selected as $L_d = 0.03\ L$, which is in a typical range of 2% to 5% in practical applications [27]; and four sensor locations are selected at the damper location, ¼ L, ½ L, and ¾ L.

3.1. CONFIGURATION AND MECHANISM OF SPAC

The proposed SPAC is an improved version of the prototype developed by the same authors [19]. An additional mechanical amplification mechanism is added to enable the SPAC to be compatible with large-scale applications, as seen in the purple frame in Fig. 2. From top to bottom, these elements are the linear rail guide, ball screw, ball nut, coupler, gearbox, EM motor, and circuit box, respectively. The circuit box contains all the necessary electrical components and is further zoomed and shown in the blue frame. The two nodes marked in red capital letters A and B correspond to the two ends of the EM motor, and are the same things in both the purple and blue frames in Fig. 2.

In terms of the circuit operation, three key modules can be subsequently identified from the blue frame, namely, (1) the **H-bridge module**, (2) the **MCU module**, and (3) the **rechargeable battery module**.

The **H-bridge module** serves as the interface between the EM motor and the rechargeable battery set. It consists of four metal–oxide–semiconductor field-effect transistors (MOSFETs, i.e., M_1 to M_4) aligned in an "H" shape from which the module obtains its name. The four MOSFETs are essentially switches that can operate at high frequencies (typically thousands of hertz or more) regulated by pulse-width modulation (PWM) signals (i.e., Sig 1 and Sig 2 in Fig. 2). An N-type MOSFET will be turned "on" when the control PWM signal is high (i.e., over trigger voltage) and "off" when PWM is low (i.e., zero voltage). When operating, the two diagonal pairs (i.e., M_1 and M_4 form one pair controlled by Sig 1, and M_2 and M_3 form the

other pair controlled by Sig 2) will be turned "on" and "off" in a rapid and consecutive manner following the signals (i.e., Sig 1 and Sig 2) outputted by a full-bridge driver (typical model: HIP 4082). The two PWM signals should always complement each other in the time domain (i.e., when Sig 1 is high, Sig 2 is low; and vice versa), which will otherwise cause a short circuit and damage the system (when both signals are high). Thus, if we define the duty cycle of Sig 1 as $D_1 = t_1/T_{PWM}$, where t_1 is the high-level duration of Sig 1 within one complete PWM wave period (T_{PWM}), then that of Sig 2 will automatically equal to $D_2 = 1- D_1$ in light of their complementary feature. By further defining that EM motor voltage V_m (positive when left node voltage is higher), battery voltage V_{batt}, circuit current i (positive when passing through the motor from right to left as shown in Fig. 2), circuit total resistance R_t, and motor inner inductance L_0, we can write the following equations for the H-bridge module within one complete PWM cycle:

$$V_m - V_{batt} - iR_t - L_0 \frac{di}{dt} = 0, \qquad \text{when } 0 < t < t_1; \tag{5}$$

$$V_m + V_{batt} - iR_t - L_0 \frac{di}{dt} = 0, \qquad \text{when } t_1 < t < T_{PWM}. \tag{6}$$

Further provided that the current change within one duty cycle must be zero, which will otherwise cause energy accumulation/leakage at the motor coil (i.e., equivalent inductor), we can derive the following equation by solving Eqs. (5) and (6)

$$i = \frac{V_m + V_{batt}(1-2D_1)}{R_t}. \tag{7}$$

Eq. (7) essentially states that the instant current passing through the motor is solely controlled by a parameter D_1, because all the other parameters are either constants (e.g., V_{batt} and R_t) or can be treated as nearly constant values (e.g., V_m) from the time scale of PWM signals. That is, motor voltage V_m normally operates at a frequency of several hertz (i.e., natural frequencies of the cable), whereas the operation frequencies of PWM signals are of thousand hertz or above. Further provided that the adopted EM motor is of non-commutated direct-current type that intrinsically follows

$$\begin{cases} V_m = K_{em}\dot{u}_d \\ f_{ctrl} = -K_{em} i \end{cases}, \tag{8}$$

the active actuation force (f_{ctrl}) can be subsequently obtained as

$$f_{ctrl} = -K_{em}\left[\frac{K_{em}\dot{u}_d + V_{batt}(1-2D_1)}{R_t}\right], \tag{9}$$

where K_{em} is known as the motor constant—an inherent constant parameter solely determined by the physical properties of the motor and remains unchanged after its manufacture; u_d is the relative displacement between the two terminals of SPAC (i.e., $\dot{u}_d$ is the relative velocity). Nevertheless, because one terminal of SPAC is fixed to the motionless ground ($u_g = 0$) and the other terminal is fixed to the cable, this relative displacement between the damper terminals (u_d) shall equal the absolute cable displacement at the damper location (u_j).

The **MCU module** can select any market-available MCU capable of receiving data, performing the calculation, and outputting control signals in a timely manner. The selected control algorithm (i.e., LQG in this paper) is first interpreted and coded in the MCU; and the MCU will subsequently process the measurements (e.g., accelerations) following the programmed code and output the control PWM signals (i.e., Sig 1 and Sig 2) to support the

normal function of the above H-bridge module following Eq. (9). In light of the potential harsh working environments for real applications in the future, the MCU can be replaced by a programmable logic controller (PLC), which is considered a more robust candidate.

The **rechargeable battery module** serves as the energy pool that will handle the energy exchange between the host structure (i.e., a bridge cable in this study) and itself. It is capable of temporarily storing the extracted energy and supplying energy back to the structure as needed. A supercapacitor may also be a promising candidate given the high-frequency charging and discharging processes that are worth future studies.

3.2. POWER ANALYSIS OF SPAC

The key feature expected from SPAC is its self-powered ability while performing active control. Thus, in this section, we will explain the fundamentals of realizing self-powered active control from the energy perspective, followed by a quantitative study.

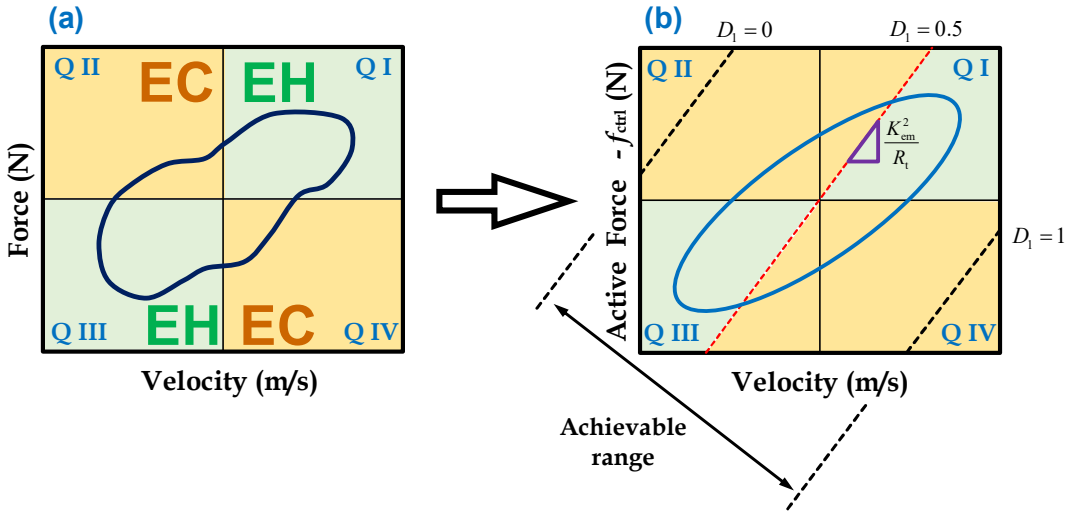

Fig. 3 Force–velocity diagrams: (a) Ideal condition with the representative contour of active control and (b) realistic diagram (reduced EH region)

Fig. 3(a) provides a typical force–velocity diagram of active control, where the entire first and third quadrants (Q I and Q III) are colored in green, suggesting potential EH regions, while the second and fourth quadrants (Q II and Q IV) are colored yellow, denoting potential EC regions. That is, the directions of the control force and the velocity are opposite to each other (i.e., dissipative force) for contours lying within EH regions (Q I and Q III) and indicate the absorption of structural kinetic energy. Conventionally, this energy portion will be dissipated as heat into the ambient environment; but with the proposed SPAC, such energy can be harvested and stored in the rechargeable battery set. Similarly, for contours in EC regions (Q II and Q IV), the control force and velocity are in the same direction, of which the process requires an external energy supply (i.e., energy supply from the battery). For a complete cycle, as long as more energy can be harvested than the consumed amount, an overall energy harvesting feature (i.e., indeed self-powered) can be guaranteed.

For quantitative analysis, following the sign definitions from Fig. 2, we learned that current flows into the battery during 0 - t_1 (i.e., charging process) and out of the battery during t_1 - T_{PWM} (i.e., EC process) within one complete PWM cycle based on the discussion in the above section. Consequently, the normalized instant power P_E can be derived as

$$P_E = V_{batt} i \left(2D_1 - 1\right). \tag{10}$$

By further substituting Eqs. (7) and (8) into Eq. (10), we can derive

$$P_E = V_m i - i^2 R_t = -f_{ctrl}\, \dot{u} - i^2 R_t. \tag{11}$$

Eq. (11) can also be directly obtained from the energy perspective because it essentially states that the total harvested energy equals the total input energy subtracting energy dissipated as heat on the circuit resistance.

Let Eq. (11) > 0, and we can obtain

$$\frac{-f_{ctrl}}{\dot{u}} < \frac{K_{em}^2}{R_t}, \tag{12}$$

which corresponds to the green-shaded area in Fig. 3(b). Compared with Fig. 3(a), the EH regions (i.e., green-colored) shrink in size in Fig. 3(b), reflecting energy loss via circuit resistance R_t, which is not considered in Fig. 3(a). Nevertheless, given that the loop can still have more of its area within the EH regions than in the EC regions, the concept of self-powered active control remains valid and feasible. Moreover, the two black dashed lines in Fig. 3(b) correspond to the scenarios wherein the duty cycle of SPAC is at its limits (i.e., $D_1 = 0$ and $D_1 = 1$ in Eq. (9)). Thus, the region between the two lines is the achievable force range, which can be enlarged by increasing battery voltage V_{batt}.

Therefore, to guarantee that the proposed system will remain self-powered in the long term ($0 \sim \tau$, where τ is the end time of the interested duration), we will only need to ensure that the accumulated energy (E) within the duration is positive, i.e.,

$$E = \int_0^\tau \left(V_m i - i^2 R_t\right) \cdot dt = \int_0^\tau \left(-f_{ctrl}\, \dot{u} - i^2 R_t\right) \cdot dt > 0. \tag{13}$$

4. CABLE STRUCTURE UNDER ACTIVE CONTROL

Thus far, we have discussed the mechanism of the SPAC and its quantitative energy analysis accordingly. In this section, we will mainly introduce how the energy index can be used to realize an adaptive self-powered active control of a cable structure.

4.1. CABLE UNDER LQG CONTROL

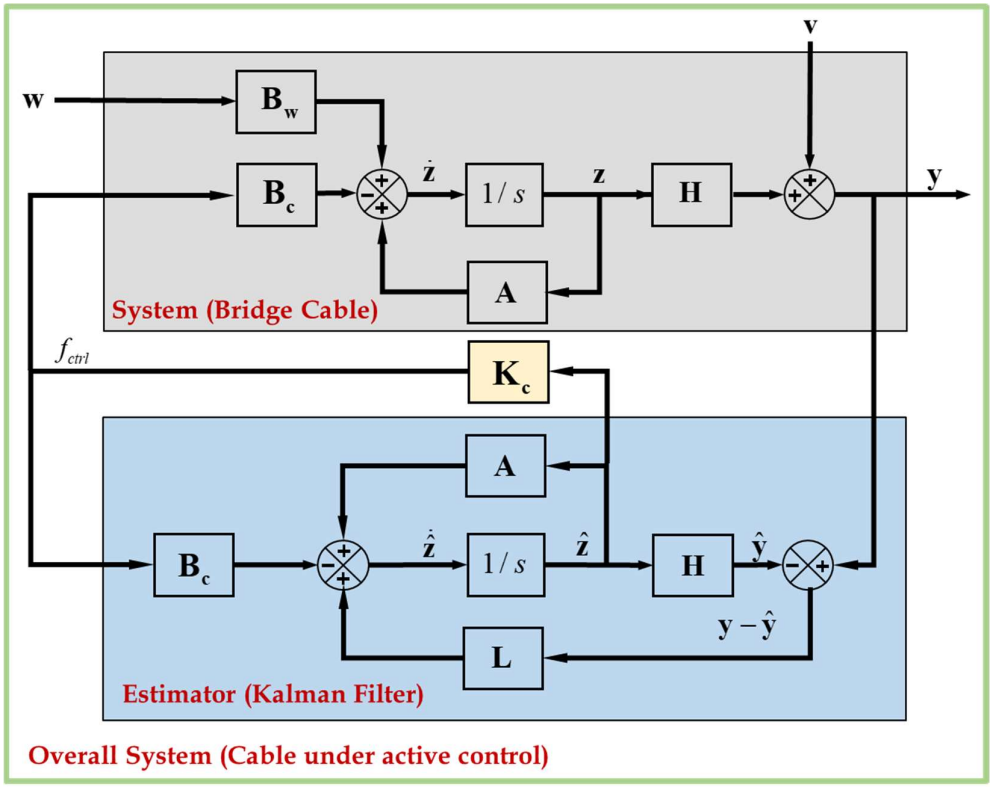

Fig. 4 Block diagram of cable under LQG control

Recall the cable with the SPAC system setup shown in Fig. 2. Only the states of the four locations where sensors are deployed are observable, thereby leading to the adoption of LQG control in this study. LQG control is merely a combination of a linear quadratic regulator (LQR) and a full-state estimator (i.e., *Kalman filter*), which can be designed separately.

A block diagram of the cable with the SPAC system under LQG control is shown in Fig. 4, where the top gray-shaded part denotes the cable system, and the bottom blue-shaded part depicts the estimator. The *Kalman filter* will estimate the full-state variable vector $\hat{\mathbf{z}}$ based on the measured output $\mathbf{y}$ that will be further multiplied by the full-state LQR gain $\mathbf{K}_c$ to generate the optimal control force to be applied to the system (i.e., plant).

Consequently, the state-space representation of the cable system (i.e., the gray-shaded part in Fig. 4) can be written as

$$\begin{cases} \dot{\mathbf{z}} = \mathbf{A}\mathbf{z} + \mathbf{B}_c f_{\text{ctrl}} + \mathbf{B}_w \mathbf{w} \\ \mathbf{y} = \mathbf{H}\mathbf{z} + \mathbf{v} \end{cases}, \tag{14}$$

where $\mathbf{z} = \begin{bmatrix} \mathbf{u} & \dot{\mathbf{u}} \end{bmatrix}^{\mathrm{T}}$ is the state vector that contains the cable displacement and velocity information; matrices $\mathbf{A}$ (system state matrix), $\mathbf{B}_c$ (input matrix for SPAC control force), and $\mathbf{B}_w$ (input matrix for external disturbances) are in the form of

$$\mathbf{A} = \begin{bmatrix} \mathbf{0} & \mathbf{I}_{n\times n} \\ -\mathbf{M}^{-1}\mathbf{K} & -\mathbf{M}^{-1}\mathbf{C} \end{bmatrix}, \mathbf{B}_c = \begin{bmatrix} \mathbf{0} \\ \mathbf{M}^{-1}\boldsymbol{\gamma} \end{bmatrix}, \mathbf{B}_w = \begin{bmatrix} \mathbf{0} \\ \mathbf{M}^{-1}\mathbf{I}_{n\times n} \end{bmatrix}. \tag{15}$$

Matrices $\mathbf{M}$, $\mathbf{C}$, $\mathbf{K}$, $\boldsymbol{\gamma}$ in Eq. (15) were previously defined in Eqs. (2)-(4). $\mathbf{y}$ is the output vector, and $\mathbf{H}$ is the observation matrix with a size of $2s \times 2n$, where s is the number of sensor locations (i.e., $s = 4$ in this study) and n is the number of the degrees of freedom (i.e., $n = 99$ in this study).

w and **v** are the external excitations (i.e., wind loads) and measurement noise, respectively. Typically, the measure noise **v** is assumed as zero-mean white noise and uncorrelated with the excitation **w**, which satisfy

$$E(\mathbf{w}\mathbf{w}^T)=\mathbf{W},\ E(\mathbf{v}\mathbf{v}^T)=\mathbf{V},\ E(\mathbf{w}\mathbf{v}^T)=0,\ E(\mathbf{v})=0\,, \tag{16}$$

where **W** and **V** are the corresponding covariances, and $E(\cdot)$ is the expectation operator. $E(\mathbf{w}\mathbf{v}^T)=0$ indicates **w** and **v** are uncorrelated.

In terms of the estimator part (the blue-shaded part), its state-space representation can be written as

$$\dot{\hat{\mathbf{z}}}=\mathbf{A}\hat{\mathbf{z}}+\mathbf{B}_{\mathbf{c}}f_{\text{ctrl}}+\mathbf{L}(\mathbf{y}-\hat{\mathbf{y}}), \tag{17}$$

where $\hat{\mathbf{y}}=\mathbf{H}\hat{\mathbf{z}}$ is the estimated output vector, and **L** is the filter gain that can be computed by

$$\mathbf{L}=\mathbf{P}\mathbf{H}^T\mathbf{V}^{-1}, \tag{18}$$

where the error covariance **P** can be solved via algebraic Riccati equation (ARE) in the form of

$$\mathbf{A}\mathbf{P}+\mathbf{P}\mathbf{A}^T+\mathbf{B}_{\mathbf{w}}\mathbf{W}\mathbf{B}_{\mathbf{w}}^T-\mathbf{P}\mathbf{H}^T\mathbf{V}^{-1}\mathbf{H}\mathbf{P}=\mathbf{0}. \tag{19}$$

Thus, the optimal estimated state vector $\hat{\mathbf{z}}$ can be computed by minimizing the following cost function:

$$J=\lim E[(\mathbf{z}-\hat{\mathbf{z}})(\mathbf{z}-\hat{\mathbf{z}})^T], \tag{20}$$

Upon successful estimation of the full-state vector $\hat{\mathbf{z}}$, the control force f_{ctrl} can be obtained as

$$f_{ctrl}=\mathbf{K}_{\mathbf{c}}\hat{\mathbf{z}}, \tag{21}$$

where $\mathbf{K}_{\mathbf{c}}$ is the LQR gain matrix (yellow block in Fig. 4) obtained by minimizing the quadratic performance index *J* in the form of

$$J=\int_0^{\infty}(\mathbf{z}^T\mathbf{Q}\mathbf{z}+f_{ctrl}^T\mathbf{R}f_{ctrl})dt\,. \tag{22}$$

where **Q** and **R** are user-defined symmetric positive definite matrices that reflect control strategies (i.e., relative weights). Consequently, $\mathbf{K}_{\mathbf{c}}$ can be calculated as

$$\mathbf{K}_{\mathbf{c}}=\mathbf{R}\mathbf{B}_{\mathbf{c}}^T\mathbf{P}_{lqr}, \tag{23}$$

where $\mathbf{P}_{lqr}$ shall always satisfy the reduced-matrix Riccati equation

$$\mathbf{A}^T\mathbf{P}_{lqr}+\mathbf{P}_{lqr}\mathbf{A}-\mathbf{P}_{lqr}\mathbf{B}_{\mathbf{c}}\mathbf{R}^{-1}\mathbf{B}_{\mathbf{c}}^T\mathbf{P}_{lqr}+\mathbf{Q}=\mathbf{0}. \tag{24}$$

In practice, the $\mathbf{K}_{\mathbf{c}}$ and **L** matrices can be computed directly using the *lqr* and *Kalman/lqe* functions in MATLAB or via other system-embedded ARE solvers in other computational environments (e.g., MCUs and PLCs).

By further defining the error vector $\mathbf{e} = \mathbf{z} - \hat{\mathbf{z}}$, and substituting Eq. (21) into Eqs. (14) and (17), we can obtain the state-space representation of the overall system (i.e., entire Fig. 4, plant with estimator) as

$$\begin{cases} \begin{bmatrix} \dot{\mathbf{z}} \\ \dot{\mathbf{e}} \end{bmatrix} = \begin{bmatrix} \mathbf{A} - \mathbf{B}_c\mathbf{K}_c & \mathbf{B}_c\mathbf{K}_c \\ \mathbf{0} & \mathbf{A} - \mathbf{LH} \end{bmatrix} \begin{bmatrix} \mathbf{z} \\ \mathbf{e} \end{bmatrix} + \begin{bmatrix} \mathbf{B}_w & \mathbf{0} \\ \mathbf{B}_w & -\mathbf{L} \end{bmatrix} \begin{bmatrix} \mathbf{w} \\ \mathbf{v} \end{bmatrix} \\ \mathbf{y} = \begin{bmatrix} \mathbf{H} & \mathbf{0} \end{bmatrix} \begin{bmatrix} \mathbf{z} \\ \mathbf{e} \end{bmatrix} \end{cases}. \tag{25}$$

4.2. CONTROL STRATEGY TO ENSURE SELF-POWERED CONTROL

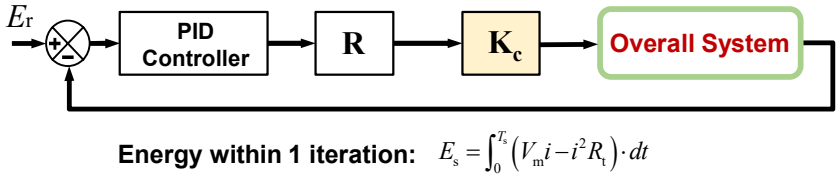

Fig. 5 Block diagram showing the adaptive strategy for ensuring the self-powered feature

The gain matrix $\mathbf{K}_c$ and the control performance is determined by the $\mathbf{Q}$ and $\mathbf{R}$ matrices in the LQG control. In this section, the $\mathbf{Q}$ matrix is set as an identity matrix $\mathbf{Q} = \mathbf{I}$, and initial $\mathbf{R}$ value is set as $\mathbf{R} = 10^{-6}$. Despite simultaneous actuation and energy harvesting abilities granted by the SPAC, active control (e.g., LQG) with a fixed gain matrix $\mathbf{K}_c$ will not necessarily guarantee the self-powered feature. That is, Eq. (13) may not always be satisfied, given the unknown excitation environment in the long run. Therefore, the gain matrix $\mathbf{K}_c$ is adaptively adjusted by tuning the $\mathbf{R}$ value.

In this regard, we further introduce a second-tier feedback loop (as shown in Fig. 5) that can update the $\mathbf{R}$ matrix periodically to tilt the relative balance between control performance and energy performance and subsequently ensures the self-powered feature. The green block in Fig. 5 represents the overall system (cable with SPAC seen in Fig. 4). With a defined new parameter–energy calculation period (T_s), the energy within each period (E_s) can be calculated using Eq. (13) and fed back to the modified proportional-integral (PI) controller to determine the $\mathbf{R}$ and then $\mathbf{K}_c$ matrices for the next iteration. $T_s = 1$ s is selected in our application because the first mode period of the selected bridge cable is also approximately 1 s. But other reasonable values (e.g., $T_s = 2$ or 3 s) will do as well. The reference energy value (E_r) in our system can be selected as zero to ensure optimal adaptive active control performance (i.e., overall energy-neutral) or an appropriate positive number to ensure the system can continuously harvest energy while providing active control. In terms of the modified PI controller block, if the error value is defined as $\delta_i = E_r - E_s$, the formula follows

$$\mathbf{R}_{n+1} = \mathbf{R}_n e^{-(K_p \delta_i + K_i \sum_{i=1}^{n} \delta_i)}, \tag{26}$$

where K_p and K_i are the proportional and integral coefficients, respectively. The updated $\mathbf{R}$ matrix will be subsequently used to derive the $\mathbf{K}_c$ matrix by following Eqs. (23) and (24).

Thus far, the power-oriented adaptive SPAC has been established; its core merit is due to the double-secured structural stability by regulating one-way energy flow under long-term operation (i.e., net energy output). As a result, the proposed system successfully addresses the

two critical issues—high power consumption and potential instability—that hinder wide industrial adoption of classic active controllers and has a promising future.

4.3. CONTROL PERFORMANCE COMPARISON: ACTIVE VERSUS PASSIVE

This section provides a qualitative control performance comparison between (1) active control using SPAC and (2) a representative passive control technique, namely, an inerter damper (ID), because neither approach requires an external energy supply.

The state-space representation of the cable with SPAC system under LQG control is derived and given in Eq. (25). Similarly, the state-space representation of the cable under ID control can be obtained from Eqs. (14) and (15) by excluding the feedback loop and updating the embedded **M** and **C** matrices to

$$\begin{cases} m_{jj}^{'} = m_{jj} + m_d \\ c_{jj}^{'} = c_{jj} + c_d \end{cases}, \tag{27}$$

where m_{jj} and c_{jj} are the j^{th} diagonal elements (i.e., damper location) in matrices **M** and **C** of the uncontrolled cable, respectively. In this study, the optimal ID parameters are searched to optimize the cable's first modal damping. More details about the optimization procedure were provided in [28, 30, 31]. Although power-oriented active control from the last section will adjust the **R** matrix continuously, a representative fixed **Q** and **R** matrices pair will be more than adequate to compare the merits over passive ID control qualitatively.

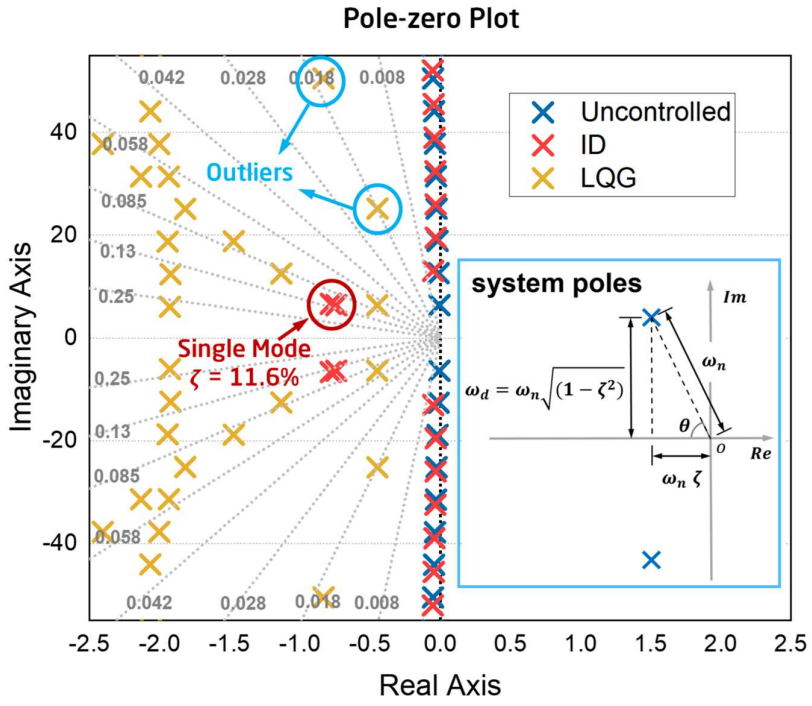

Fig. 6 System poles under various conditions

Fig. 6 provides the pole-zero diagram of the cable system under three different conditions, namely, uncontrolled, with ID, and with active control (i.e., LQG), as marked in the legend. The system poles are essentially eigenvalues of the system matrix **A** and are denoted by cross symbols distinguishable by colors. As explained in the blue-framed subfigure in Fig. 6, the system poles contain information on both modal frequencies and the corresponding damping

ratios. The coordinates of a pole can be read at ($\omega_n\zeta$, $\omega_n\sqrt{1-\zeta^2}$), where ζ is the damping ratio, ω_n is the modal natural frequency. ζ can be calculated as $\zeta = \cos(\theta)$, where θ is the angle between the pole and the *x*-axis. To facilitate the figure interpretation, polarized gray dotted grid lines are provided with corresponding damping ratios.

From the figure, we can tell that all poles of the uncontrolled case (blue-colored) lie close to the $x = 0$ line, indicating all modes are of extremely low damping ratios (the inherent damping is less than 0.8%,). In contrast, two nearly overlapping pole sets (red-colored) lying far from the $x = 0$ line to the left can be identified from the ID control case, whereas the rest of the poles have similar positions to those in the uncontrolled case. The observed overlapping poles indicate the merging of the first and second modes due to ID, the merged poles correspond to the original first mode, and the new third mode recedes to the original second mode, etc. Consequently, only the first mode of the cable has a high damping ratio ($\zeta_1 = 11.6\%$ as identified in Fig. 6), leaving the rest of the modes nearly uncontrolled.

The system poles of active LQG control consist of two groups: the eigenvalues of $\mathbf{A} - \mathbf{B}_c\mathbf{K}_c$ (*control poles*) and those of $\mathbf{A} - \mathbf{LH}$ (*estimator poles*). In terms of system control performance, only the *control poles* will determine the corresponding modal damping ratios, which all lie between the $\zeta = 5.8\%$ and $\zeta = 8.5\%$ lines, yet with two outliers. The two outliers stem from the sensor arrangement issue because all the sensors, except for the one at the damper location, are at their stationary points for the fourth and eighth modes, making no contribution to the estimation process. Nevertheless, other than the two outliers, all the other modes have high damping ratios, suggesting a successful realization of simultaneous multi-mode vibration control by SPAC.

5. Numerical Simulation and Result Discussion: A Case Study

This section will conduct a comprehensive numerical study on the control performance of the proposed SPAC system to a cable structure.

5.1. Cable Information

A 135 m full-scale cable from [28] is adopted as the benchmark cable in this study. Relevant parameters of both the cable and the adopted EM motor of SPAC are provided in Table 1. The cable is discretized into 99 degrees of freedom (i.e., $n = 99$) for numerical validation.

Table 1 Parameters of the benchmark cable and EM motor

Parameters	Symbol	Value	
Benchmark Cable			
Cable length	L	135	m
Damper position	L_d	$0.03L$	m
Cable outer diameter	D	85	mm
Cable mass per unit length	m	16.65	kg/m
Cable tension force	T	1,200	kN
Young's modulus	E	1.95×10^{11}	N/m^2
Fundamental frequency	f_1	1.08	Hz

Cable inherent damping ratio	ζ_c	0.1 %	-
EM motor			
Motor constant	K_{em}	1,000	N/A or V−s/m
Circuit total resistance	R_t	10	Ω
Motor inductance	L_t	0.03	H

5.2. DYNAMIC RESPONSE SIMULATION

Turbulent wind loads with a reference mean speed of 10 m/s (measured 10 m above sea level) are generated using the spectral representation method with a time step of 1/64 s, in which the frequency bandwidth ranges between 0 to 8 Hz, covering the first 7 modes of the selected cable. Such wind loads are converted into lumped node forces (a total of $n = 99$ nodes) in the time domain and are subsequently adopted in the upcoming simulations. Fig. 7 provides the corresponding wind force time history of one selected node, i.e., the 40th node at 0.4L location. Details on the wind load generation process can be found in Appendix I of reference [6].

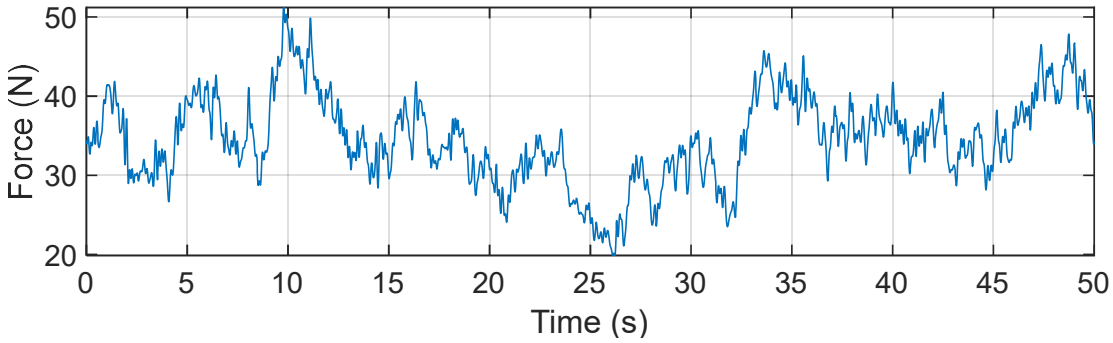

Fig. 7 Wind force time history of the 40th node (total node $n = 99$, mean wind speed = 10 m/s)

For the comparison case with ID installed at 0.03 L location, the optimal inertance damping coefficients were determined as b_d = 8,130 kg, and c_d = 26 kN−s/m following the optimization method introduced in [28]; the corresponding optimal damping ratio for the first mode (ζ_1) can be calculated as 11.6%, matching the reading from Fig. 6.

The EM motor listed in Table 1 is adopted in the SPAC to perform the adaptive active control (i.e., LQG).

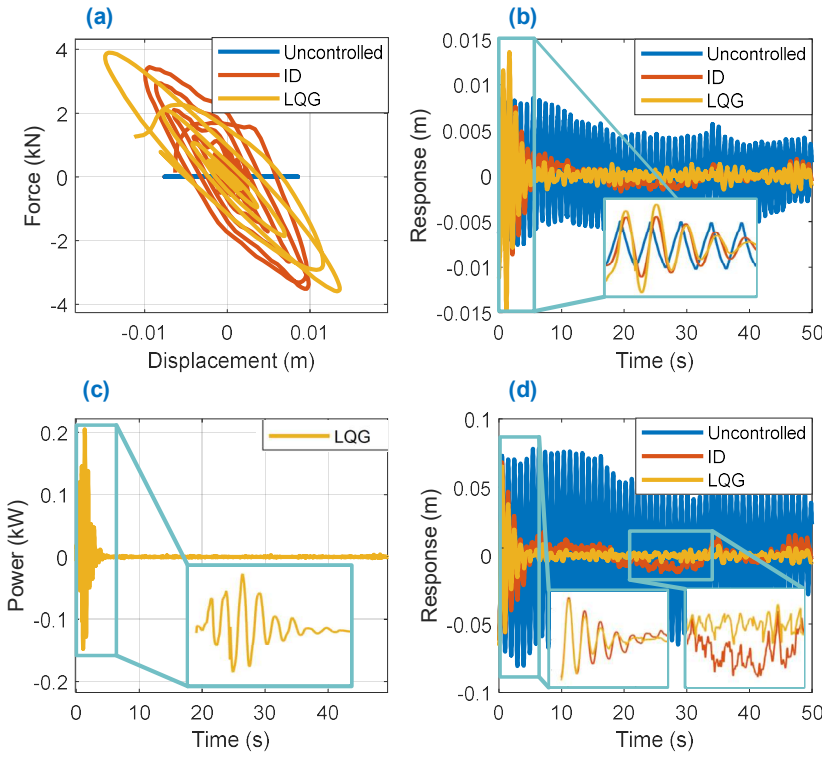

Fig. 8 Cable simulation results (a) damper force-displacement diagram (b) Cable responses at damper location (c) Instant power in time domain (d) cable responses at 0.4*L* location

Fig. 8(a) shows the hysteresis loops of all three cases (i.e., uncontrolled, ID, and LQG control), where both the ID and LQG control cases have negative slopes in the force-displacement hysteresis loops. Intuitively, such a negative stiffness feature will amplify the vibration amplitude at the damper location, which is considered beneficial to local energy accumulation. That is, kinetic energy from other parts of the cable will be diverted to the damper location. This energy accumulation will lead to more efficient energy dissipation via the damper (either through ID or SPAC) and subsequently results in better overall cable vibration control performance.

Fig. 8(b) provides the cable responses at the damper location. The response of the LQG control case is larger than that of ID control in the initial state (i.e., the first 2 seconds, as illustrated in the zoomed subfigure). On the basis of the above discussion, we learned this larger vibration amplitude of LQG control corresponds to a more effective energy dissipation ability that will subsequently leads to better overall cable control performance. This claim is cross supported by the simulation results from Fig. 8(d), where the response of LQG control at the 0.4 *L* location is smaller than that of ID control. We would like to emphasize that this LQG control is the power-oriented adaptive self-powered active control realized by the SPAC that requires no external supply.

Fig. 8(c) shows a diagram of the instant power exchanged between the cable and the rechargeable battery set of the SPAC in the time domain. A positive value indicates a power flow from the cable to the battery (i.e., energy harvesting process), whereas a negative value suggests a reverse energy flow that drains energy from the battery to support the actuation process. Nevertheless, with the proposed power-oriented strategy covered in Section 4.2, the

overall accumulated energy (covered area – i.e., integration of instant power) is kept at zero or a positive value to enable long-term self-powered active control.

Fig. 8(d) depicts the cable responses at the 0.4 L location. In addition to the enhanced vibration amplitude mitigation performance of LQG control than the ID control, as mentioned above, the response of LQG control is also observed to be "smoother" (seen in the right subfigure). This condition can be explained by the simultaneous multi-mode vibration control ability covered in Section 4.3, because the burrs are mainly contributed by the superposition of higher modes. The root mean square response of the ID case can be subsequently calculated as 0.0119 m, whereas that of LQG scenario is 0.0102 m, indicating the improvement of an additional 14.3% response reduction (i.e., LQG over ID).

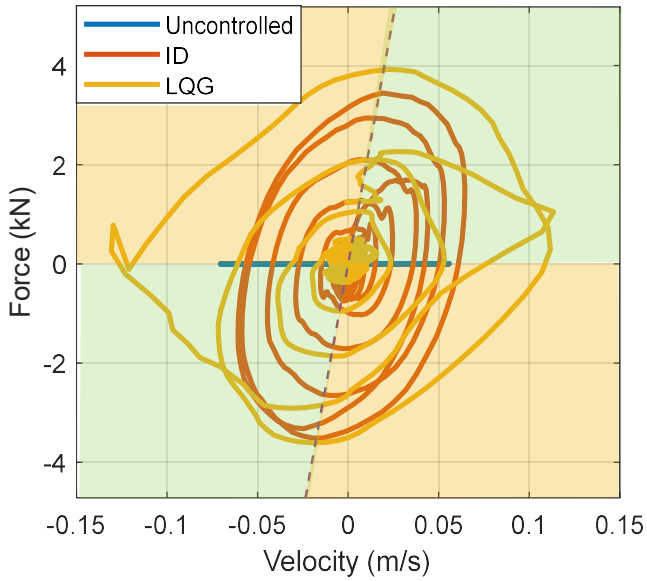

Fig. 9 Force velocity diagram under various conditions

Fig. 9 shows the corresponding force–velocity diagrams at the damper location. As previously explained in Fig. 3, the contour within the green region indicates the SPAC is harvesting energy from the cable. In contrast, the portion lying in the yellow region will require energy supply from the battery to return to the cable for overall better control performance. With the introduced adaptive strategy, the self-powered SPAC will dynamically balance the trajectories in the green and yellow zones to ensure an overall self-powered active control.

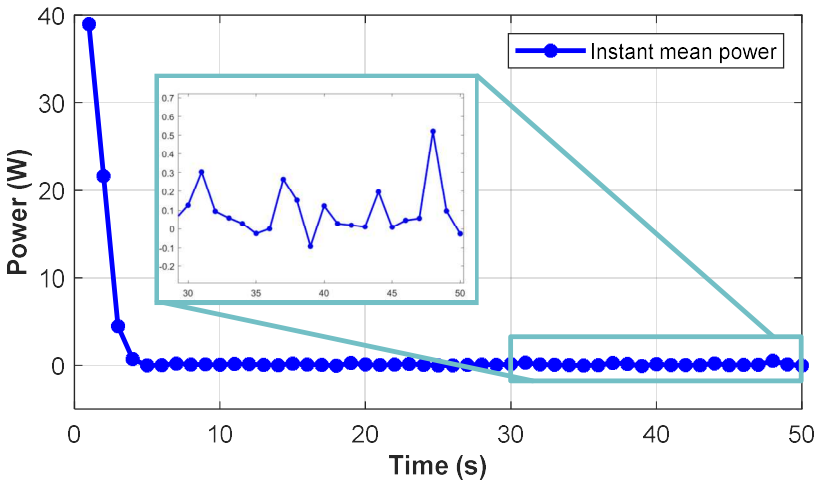

Fig. 10 Mean power in the time domain

Fig. 10 provides the time history of the instant mean power. The *instant mean power* stands for the mean power calculated within on iteration period (i.e., E_s / T_s), and the comparative fluctuation nature of the *instant mean power* results from the adaptive control strategy detailed in Section 4.2 (i.e., the **R** matrix is updated after every iteration).

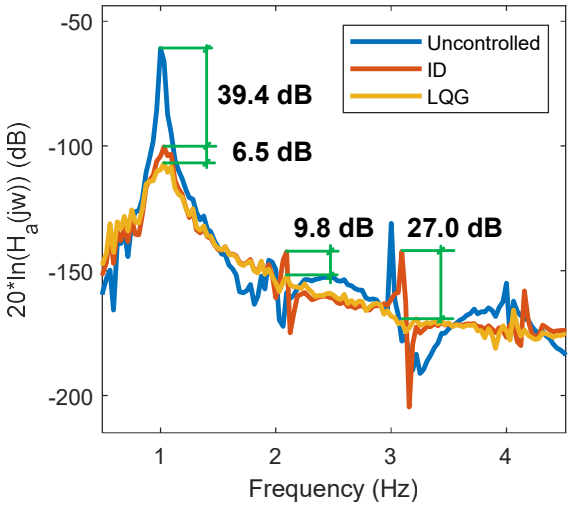

Fig. 11 Response at 0.4*L* in frequency domain

The responses at 0.4 L of the three scenarios in the frequency domain are provided in Fig. 11. The simulations are performed under the same wind excitation series. The four clusters of peaks correspond to the first four natural frequencies of the cable. For the first mode control, a significant amplitude reduction of 39.4 dB is achieved by the optimal ID case compared with the uncontrolled case, and an additional 6.5 dB reduction is further realized by the proposed SPAC compared with the optimal ID case. As aforementioned, because the ID control was optimized for first-mode control only, LQG control using SPAC successfully achieved significant amplitude reduction for the second and third mode controls at 9.8 dB and 27 dB, respectively, whereas the response amplitudes of ID control are of similar heights to those of the uncontrolled case. The compromised control performance of SPAC at the fourth mode is due to the previously mentioned sensor arrangement issue, which can be easily improved by

changing the sensor locations. Nevertheless, the wide-band low profile of the LQG curve indicates the overall superior control performance of the proposed SPAC system.

6. Conclusion

This paper presents a feasibility study on the implementation of a novel power-oriented adaptive self-powered active control system to bridge cable for enhanced vibration mitigation performance. A 135 m full-scale bridge stay cable model under high-speed wind load (25m/s) was selected as the demonstration example. On the basis of combined analytical and numerical simulation results, the major conclusions can be drawn as follows:

1. In this paper, we successfully integrated a power-oriented control strategy with the novel full-loop self-powered active controller, leading to the formation of a new control system: a long-term adaptive self-powered active control system.
2. The newly proposed system successfully resolves the two long-lasting concerns associated with traditional active control (i.e., high power consumption and potential instability) without compromising control performance.
3. The feasibility and effectiveness of the newly proposed system are systematically validated via a case study by exerting control on a full-scale bridge cable structure. An additional 6.5 dB, 9.8 dB, and 27 dB amplitude reduction were successfully achieved for the first three modes compared with those using an optimal ID.

7. Acknowledgments

The authors are thankful for the financial support provided by the Research Grants Council of Hong Kong (Nos. PolyU 15214620, PolyU R5020-18, and T22-502/18-R) and the National Observation and Research Station of Material Corrosion and Structural Safety of Hong Kong-Zhuhai-Macao Bridge in Guangdong. The first author gratefully acknowledges the financial support from the Postdoc Matching Fund Scheme of The Hong Kong Polytechnic University (PP0034914). The findings and opinions expressed in this paper are those of the authors alone and are not necessarily the views of the sponsors.

References

[1] G. W. Housner *et al.*, "Structural Control: Past, Present, and Future," *Journal of Engineering Mechanics,* vol. 123, no. 9, pp. 897-971, 1997, doi: 10.1061/(asce)0733-9399(1997)123:9(897).

[2] R. Zhang, X. Wang, and S. John, "A Comprehensive Review of the Techniques on Regenerative Shock Absorber Systems," *Energies,* vol. 11, no. 5, pp. 1-43, 2018, doi: 10.3390/en11051167.

[3] Q. Cai and S. Zhu, "The nexus between vibration-based energy harvesting and structural vibration control: A comprehensive review," *Renewable and Sustainable Energy Reviews,* p. 111920, 2021.

[4] W. Shen, S. Zhu, Y.-L. Xu, and H.-P. Zhu, "Energy regenerative tuned mass dampers in high-rise buildings," *Structural Control and Health Monitoring,* vol. 25, no. 2, pp. 1-18, 2018, doi: 10.1002/stc.2072.

[5] L. Zuo and W. Cui, "Dual-Functional Energy-Harvesting and Vibration Control: Electromagnetic Resonant Shunt Series Tuned Mass Dampers," *Journal of Vibration and Acoustics,* vol. 135, no. 5, pp. 051018-051018, 2013/06/18/ 2013, doi: 10.1115/1.4024095.

[6] W. Shen and S. Zhu, "Harvesting energy via electromagnetic damper: Application to bridge stay cables," *Journal of Intelligent Material Systems and Structures,* vol. 26, no. 1, pp. 3-19, 2015, doi: 10.1177/1045389x13519003.
[7] W. Shen, S. Zhu, and H. Zhu, "Experimental study on using electromagnetic devices on bridge stay cables for simultaneous energy harvesting and vibration damping," *Smart Mater Struct,* vol. 25, no. 1, pp. 1-17, 2016, doi: doi:10.1088/0964-1726/25/6/065011.
[8] W. Shen, Z. Sun, Y. Hu, L. Cai, H. Zhu, and S. Silva, "Energy harvesting performance of an inerter-based electromagnetic damper with application to stay cables," *Mechanical Systems and Signal Processing,* vol. 170, p. 108790, 2022-05-01 2022, doi: 10.1016/j.ymssp.2021.108790.
[9] S.-W. Cho, H.-J. Jung, and I.-W. Lee, "Smart passive system based on magnetorheological damper," *Smart Mater Struct,* vol. 14, no. 4, pp. 707-714, 2005, doi: 10.1088/0964-1726/14/4/029.
[10] I.-H. Kim, H.-J. Jung, and J.-H. Koo, "Experimental evaluation of a self-powered smart damping system in reducing vibrations of a full-scale stay cable," *Smart Mater Struct,* vol. 19, no. 11, p. 115027, 2010, doi: 10.1088/0964-1726/19/11/115027.
[11] C. Chen and W. H. Liao, "A self-sensing magnetorheological damper with power generation," (in English), *Smart Mater Struct,* vol. 21, no. 2, Feb 2012, doi: 10.1088/0964-1726/21/2/025014.
[12] J. T. Scruggs and W. D. Iwan, "Structural control with regenerative force actuation networks," *Structural Control and Health Monitoring,* vol. 12, no. 1, pp. 25-45, 2005, doi: 10.1002/stc.50.
[13] Y. Suda, S. Nakadai, and K. Nakano, "Hybrid Suspension System with Skyhook Control and Energy Regeneration (Development of Self-Powered Active Suspension)," *Vehicle System Dynamics,* vol. 29, no. sup1, pp. 619-634, 1998, doi: 10.1080/00423119808969590.
[14] X. Tang and L. Zuo, "Simultaneous energy harvesting and vibration control of structures with tuned mass dampers," *Journal of Intelligent Material Systems and Structures,* vol. 23, no. 18, pp. 2117-2127, 2012, doi: 10.1177/1045389x12462644.
[15] M. Jamshidi, C. Chang, and A. Bakhshi, "Self-powered hybrid electromagnetic damper for cable vibration mitigation," *Smart Structures and Systems,* vol. 20, no. 3, pp. 285-301, 2017.
[16] M. Jamshidi, C.-c. Chang, and A. Bakhshi, "Design and control of a self-powered hybrid electromagnetic damper," *Journal of Sound and Vibration,* vol. 428, pp. 147-167, 2018, doi: 10.1016/j.jsv.2018.05.004.
[17] S.-A. Chen, X.-D. Jiang, M. Yao, S.-M. Jiang, J. Chen, and Y.-X. Wang, "A dual vibration reduction structure-based self-powered active suspension system with PMSM-ball screw actuator via an improved H2/H∞ control," *Energy,* vol. 201, 2020, doi: 10.1016/j.energy.2020.117590.
[18] J.-Y. Li and S. Zhu, "Tunable electromagnetic damper with synthetic impedance and self-powered functions," *Mechanical Systems and Signal Processing,* vol. 159, 2021, doi: 10.1016/j.ymssp.2021.107822.
[19] J.-Y. Li and S. Zhu, "Self-Powered Active Vibration Control: Concept, Modeling, and Testing," *Engineering,* vol. 11, pp. 126-137, 2022, doi: 10.1016/j.eng.2021.03.022.
[20] Y. Fujino, P. Warnitchai, and B. Pacheco, "Active stiffness control of cable vibration," *Journal of Applied Mechanics,* 1993.
[21] J.-C. Chen, "Response of large space structures with stiffness control," *Journal of Spacecraft and Rockets,* vol. 21, no. 5, pp. 463-467, 1984.
[22] Y. Fujino and T. Susumpow, "An experimental study on active control of in-plane cable vibration by axial support motion," *Earthquake engineering & structural dynamics,* vol. 23, no. 12, pp. 1283-1297, 1994.
[23] Y. Achkire and A. Preumont, "Active tendon control of cable-stayed bridges," *Earthquake engineering & structural dynamics,* vol. 25, no. 6, pp. 585-597, 1996.
[24] Y. Achkire, "Active tendon control of cable-stayed bridges," Ph.D. Thesis, Universit´e Libre de Bruxelles, 1997.

[25] F. Bossens and A. Preumont, "Active tendon control of cable-stayed bridges: a large-scale demonstration," *Earthquake Engineering & Structural Dynamics,* vol. 30, no. 7, pp. 961-979, 2001-07-01 2001, doi: 10.1002/eqe.40.
[26] A. Preumont, M. Voltan, A. Sangiovanni, B. Mokrani, and D. Alaluf, "Active tendon control of suspension bridges," *Smart Struct. Syst,* vol. 18, no. 1, pp. 31-52, 2016.
[27] X. Shi, S. Zhu, and S. Nagarajaiah, "Performance Comparison between Passive Negative-Stiffness Dampers and Active Control in Cable Vibration Mitigation," *Journal of Bridge Engineering,* vol. 22, no. 9, pp. 1-15, 2017, doi: 10.1061/(asce)be.1943-5592.0001088.
[28] J.-Y. Li, S. Zhu, X. Shi, and W. Shen, "Electromagnetic Shunt Damper for Bridge Cable Vibration Mitigation: Full-Scale Experimental Study," *Journal of Structural Engineering,* vol. 146, no. 1, 2020, doi: 10.1061/(asce)st.1943-541x.0002477.
[29] A. B. Mehrabi and H. Tabatabai, "Unified Finite Difference Formulation for Free Vibration of Cables," *Journal of Structural Engineering,* vol. 124, no. 11, pp. 1313-1322, 1998, doi: 10.1061/(asce)0733-9445(1998)124:11(1313).
[30] Y. Li, W. Shen, and H. Zhu, "Vibration mitigation of stay cables using electromagnetic inertial mass dampers: Full-scale experiment and analysis," *Engineering Structures,* vol. 200, no. 1, pp. 1-18, 2019, doi: 10.1016/j.engstruct.2019.109693.
[31] X. Shi and S. Zhu, "Dynamic characteristics of stay cables with inerter dampers," *Journal of Sound and Vibration,* vol. 423, pp. 287-305, 2018, doi: 10.1016/j.jsv.2018.02.042.